Energy & Environmental Science

ROYAL SOCIETY OF CHEMISTRY

PAPER

View Article Online
View Journal

Cite this: DOI: 10.1039/d0ee01968b

Methanol tolerance of atomically dispersed single metal site catalysts: mechanistic understanding and high-performance direct methanol fuel cells†

Qiurong Shi,‡[a] Yanghua He,‡[a] Xiaowan Bai,‡[b] Maoyu Wang,[c] David A. Cullen,[d] Macros Lucero,[c] Xunhua Zhao,[b] Karren L. More,[d] Hua Zhou,[e] Zhenxing Feng,*[c] Yuanyue Liu*[b] and Gang Wu*[a]

Proton-exchange membrane fuel cells (PEMFCs) and direct methanol fuel cells (DMFCs) are promising power sources from portable electronic devices to vehicles. The high-cost issue of these low-temperature fuel cells can be primarily addressed by using platinum-group metal (PGM)-free oxygen reduction reaction (ORR) catalysts, in particular atomically dispersed metal–nitrogen–carbon (M–N–C, M = Fe, Co, Mn). Furthermore, a significant advantage of M–N–C catalysts is their superior methanol tolerance over Pt, which can mitigate the methanol cross-over effect and offer great potential of using a higher concentration of methanol in DMFCs. Here, we investigated the ORR catalytic properties of M–N–C catalysts in methanol-containing acidic electrolytes *via* experiments and density functional theory (DFT) calculations. FeN_4 sites demonstrated the highest methanol tolerance ability when compared to metal-free pyridinic N, CoN_4, and MnN_4 active sites. The methanol adsorption on MN_4 sites is even strengthened when electrode potentials are applied during the ORR. The negative influence of methanol adsorption becomes significant for methanol concentrations higher than 2.0 M. However, the methanol adsorption does not affect the $4e^-$ ORR pathway or chemically destroy the FeN_4 sites. The understanding of the methanol-induced ORR activity loss guides the design of promising M–N–C cathode catalyst in DMFCs. Accordingly, we developed a dual-metal site Fe/Co–N–C catalyst through a combined chemical-doping and adsorption strategy. Instead of generating a possible synergistic effect, the introduced Co atoms in the first doping step act as ''scissors'' for Zn removal in metal–organic frameworks (MOFs), which is crucial for modifying the porosity of the catalyst and providing more defects for stabilizing the active FeN_4 sites generated in the second adsorption step. The Fe/Co–N–C catalyst significantly improved the ORR catalytic activity and delivered remarkably enhanced peak power densities (*i.e.*, 502 and 135 mW cm^{-2}) under H_2–air and methanol–air conditions, respectively, representing the best performance for both types of fuel cells. Notably, the fundamental understanding of methanol tolerance, along with the encouraging DMFC performance, will open an avenue for the potential application of atomically dispersed M–N–C catalysts in other direct alcohol or ammonia fuel cells.

Received 19th June 2020,
Accepted 17th August 2020

DOI: 10.1039/d0ee01968b

rsc.li/ees

[a] *Department of Chemical and Biological Engineering, University at Buffalo, The State University of New York, Buffalo, NY 14260, USA. E-mail: gangwu@buffalo.edu*
[b] *Texas Materials Institute and Department of Mechanical Engineering, The University of Texas at Austin, Austin, Texas 78712, USA. E-mail: Yuanyue.liu@austin.utexas.edu*
[c] *School of Chemical Biological, and Environmental Engineering Oregon State University, Corvallis, OR 97331, USA. E-mail: Zhenxing.feng@oregonstate.edu*
[d] *Center for Nanophase Materials Sciences, Oak Ridge National Laboratory, Oak Ridge National Laboratory, Oak Ridge, TN 37831, USA*
[e] *X-Ray Science Division, Argonne National Laboratory, Lemont, IL, 60439, USA*

† Electronic supplementary information (ESI) available. See DOI: 10.1039/d0ee01968b

‡ These authors contributed equally.

Broader context

Hydrogen proton-exchange membrane fuel cells (PEMFCs) and direct methanol fuel cells (DMFCs), which both use low-temperature acidic PEMs as electrolytes, are promising power sources for a variety of applications from portable electronics to electric vehicles. The development of high-performance platinum group metal (PGM)-free catalysts is in high demand to address the high-cost issue of PEMFCs. Among studied PGM-free formulations, atomically dispersed M–N–C (M: Fe, Co, or Mn) catalysts have exhibited encouraging catalytic activity and stability for the oxygen reduction reaction (ORR). Importantly, they have superior methanol tolerance during the ORR when compared to traditional Pt catalysts, which is ideal for the ORR cathode in DMFCs. This work provides an insightful understanding of methanol adsorption behavior on these PGM-free CN_x and MN_4 sites for rational catalyst design to improve the DMFC performance. As a result, an innovative dual-site Fe/Co–N–C catalyst with an increased density of active sites and favorable porosity achieved exceptional power densities in both H_2– and methanol–air cells. Beyond H_2, this work demonstrated the excellent feasibility of using atomically dispersed M–N–C catalysts for direct alcohol or ammonia fuel cells.

Introduction

Currently, the global environmental pollution issues and fossil fuel crisis have been increasingly exacerbated. This inspired extensive research on developing sustainable and renewable electrochemical energy conversion technologies, including proton-exchange membrane fuel cells (PEMFCs), direct methanol fuel cells (DMFCs), and water electrolyzers.[1–4] Numerous efforts have been devoted to the study of PEMFCs due to their relatively high efficiency and environmentally-benign properties for applications majorly in electric vehicles. Alternatively, DMFCs are attractive for applications of portable electronics due to their high energy density and easy storage/transport of methanol.[5–9] In both PEMFCs and DMFCs, the advancement of the oxygen reduction reaction (ORR) cathode catalysts is vitally crucial for promoting their overall performance. The exorbitant cost, insufficient durability, and the inferior methanol/impurity tolerance of current platinum group metal (PGM) catalysts largely hindered the wide applications of fuel cells.[10] Recently, PGM-free catalysts, especially the atomically dispersed M–N–C (M = Fe, Co, Mn) material, have exhibited encouraging activity and stability in acidic media, holding great promise as ORR cathode catalysts.[6,11–21] Importantly, the methanol tolerance of M–N–C catalysts endows them with a significant advantage for DMFCs.[6,9,22–25] The serious methanol cross-over from the anode to the cathode resulted in significant performance loss at the Pt/C cathode, remaining a grand challenge for DMFCs. The methanol cross-over dramatically reduces the overall cell voltage due to a mixed potential generated from the simultaneous ORR and methanol oxidation reaction (MOR). Methanol also poisons Pt sites and inhibits their catalytic performance at the cathode. The cross-over becomes aggravated with an increase of the methanol concentration, which impedes the use of methanol with high concentrations for achieving high-power DMFCs.

Among studied M–N–C catalysts,[12,26,27] Fe–N–C materials, consisting of FeN_4 active sites embedded into carbon planes, demonstrated the best activity toward ORR in acidic electrolytes.[8,9,14,15,28,29] Tremendous efforts have been focusing on the modifications of the local coordination environment and atomic structure of active sites and the overall morphology of catalysts for enhancing performance and durability.[12,18,28,30–33] Nevertheless, the membrane electrode assembly (MEA) performance and durability of current Fe–N–C cathodes under H_2–air conditions are still insufficient for practical applications. Alternatively, the application of M–N–C catalysts in DMFCs could be more attractive.[34,35] Due to kinetically slow methanol oxidation at the anode, the M–N–C cathode can easily generate a sufficient current density to match. Therefore, the relatively low performance of M–N–C cathodes could not be the major limitation in DMFCs. Many groups, including us, have made a significant contribution to engineering Fe–N–C cathode in boosting DMFC performance.[6,8,9,22] However, the power density of the methanol–air cell is still far away from the U.S. DOE's target of 250 mW cm^{-2}. Besides, fundamental studies on M–N–C catalysts in terms of their methanol tolerance behavior, methanol adsorption on active sites, and methanol cross-over effect on the MEA performance are still lacking in the field, which is of great importance in guiding the rational design of advanced M–N–C catalysts for DMFC applications.

Here, we conducted fundamental studies using a well-defined atomically dispersed Fe–N–C catalyst, exclusively containing FeN_4 active sites,[36] which aims to convey insightful understanding toward the methanol-induced ORR catalytic behavior. Combined with a theoretical study, we revealed that FeN_4 sites exhibited the weakest methanol adsorption relative to other PGM-free active sites, including pyridinic N, CoN_4, and MnN_4. The methanol adsorption on MN_4 sites is involved with the electrochemical process and is strengthened when potentials are applied for the ORR. However, methanol adsorption does not affect the $4e^-$ ORR pathway and damage the structure of the FeN_4 site. Based on the understanding, we accordingly designed and synthesized an atomically dispersed dual-site Fe/Co–N–C catalyst *via* an innovative two-step chemical-doping and adsorption strategy, demonstrating improved catalytic performance and mass transport in DMFCs. Compared to conventional single metal sites, a dual-metal site may provide a new opportunity to design M–N–C catalysts with enhanced intrinsic activity and stability due to optimal modifications of local geometric and electronic structures.[37] Wang *et al.* have reported a dual-site (Fe,Co)–N–C catalyst to enhance the intrinsic activity of FeN_x sites through a synergistic effect.[38] In contrast, in our work, instead of generating a synergistic effect, the doped Co species in the first step act as ''scissors'' for Zn removal during the carbonization of zeolitic imidazolate framework-8 (ZIF-8) precursors to create more defects, which is crucial for generating FeN_4 active sites in the second adsorption step with favorable porosity. The Fe/Co–N–C catalyst yielded promising intrinsic ORR activity in acidic electrolytes with a

half-wave potential ($E_{1/2}$) of 0.85 V *vs.* RHE. Importantly, in MEAs, it demonstrated a record power density of 502 and 135 mW cm^{-2} in H_2– and methanol–air cells, respectively, representing the best performance so far for both types of fuel cells.

Results and discussion

Mechanistic studies of the ORR in the presence of methanol

We employed an Fe–N–C catalyst exclusively containing FeN_4 active sites as an ideal model to study the effect of the methanol concentration on the ORR in acidic electrolytes. As shown in the high-angle annular dark-field scanning electron microscopy (HAADF-SEM) and scanning transmission electron microscopy (STEM) image (Fig. S1, ESI†), the Fe–N–C catalyst is featured with typical atomically dispersed single Fe sites and displayed a uniform carbon particle size distribution of about 65 nm. Importantly, its sufficient ORR catalytic activity and stability (Fig. S2, ESI†) are perfect for fundamental studies on the methanol tolerance of FeN_4 active sites.

The Fe–N–C catalyst exhibited negligible activity changes (*i.e.*, a 3 mV $E_{1/2}$ shift) when the methanol concentration is below 2.0 M in O_2-saturated 0.5 M H_2SO_4 electrolyte (Fig. 1A). However, when the methanol concentration is over 2.0 M, it showed noticeable activity degradation. The activity could not be recovered by transferring the RDE working electrode from the methanol-containing electrolyte to the methanol-free one (Fig. 1B and C and Fig. S3, ESI†). This suggests that methanol could be firmly adsorbed on the FeN_4 active sites and affect the ORR activity. In principle, the presence of methanol promotes O_2 solubility and diffusion coefficient in electrolytes, which should improve the ORR. For example, when the methanol concentration reached 16.0 M (Fig. S3C, ESI†), the diffusion limited current increased sharply. That is caused by the significant increase in the O_2 diffusion coefficient and the solubility in the electrolyte containing a high concentration of methanol.[39,40] Thus, the observed ORR activity loss in the presence of methanol in the kinetic range is likely due to the adsorption on FeN_4 active sites or adjacent carbon. Regardless of with or without methanol, the ORR on FeN_4 sites still follows the 4 electron pathway with negligible H_2O_2 yields (Fig. 1D). It indicates that the presence of methanol does not change the ORR catalysis pathway or destroy the structure of FeN_4 sites.[41] To further prove that most of the FeN_4 sites are free and remain intact, we further added KSCN to the methanol-free H_2SO_4 electrolyte to study the Fe–N–C catalyst that was already degraded in the methanol-containing electrolyte. We found that the ORR activity suffered from a severe degradation (Fig. S4A, ESI†), which is similar to the $E_{1/2}$ decay when the fresh Fe–N–C catalyst was directly tested in KSCN-containing electrolyte (Fig. S4B, ESI†). That means that the methanol adsorption on the FeN_4 sites is not strong enough to block SCN^- ions. The poisoning of SCN^- ions on FeN_4 sites easily causes significant activity loss for the ORR.

Fe–N–C catalysts usually contain two types of active sites for ORR electrocatalysis: FeN_4 moieties and metal-free pyridinic N.[42] To discriminate the likely methanol adsorption sites, a methanol tolerance study was also conducted by using a ZIF-8 derived N–C catalyst, which majorly contains dominant pyridinic N dopants. The N–C catalyst exhibited significant activity loss, *i.e.*, 21 mV and 37 mV negative shifts of $E_{1/2}$, much higher than those of Fe–N–C, in acidic electrolytes with 1.0 and 2.0 M methanol, respectively (Fig. 1E). Thus, methanol is more easily adsorbed onto pyridinic N sites than FeN_4 sites. After the

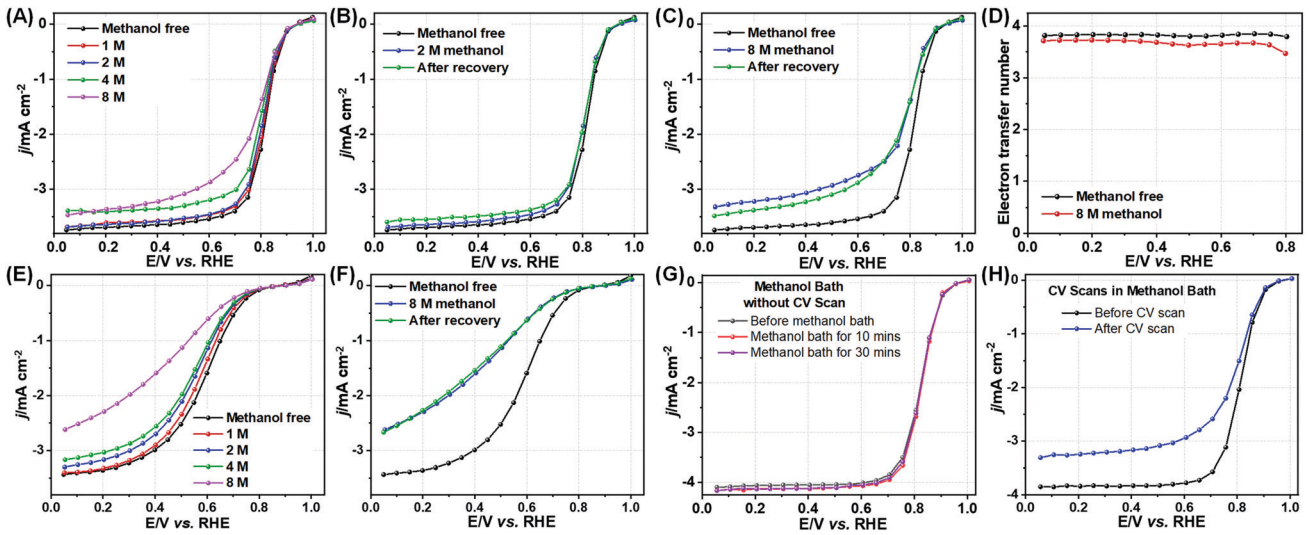

Fig. 1 ORR polarization plots of the Fe–N–C catalysts in O_2 saturated 0.5 M H_2SO_4 aqueous solution containing different methanol concentrations (A) and their selected rinse recovery polarization plots obtained by transferring the electrode in a methanol-free electrolyte (B and C) with a rotation rate of 900 rpm. (D) Electron transfer number of Fe–N–C catalysts in O_2-saturated 0.5 M H_2SO_4 electrolyte without and with 8 M methanol, respectively. ORR polarization plots of the ZIF-8-derived N–C catalyst in O_2-saturated 0.5 M H_2SO_4 solution containing different methanol concentrations (E) and the selected recovery in methanol-free electrolyte (F) with a rotation rate of 900 rpm. ORR polarization plots of the Fe–N–C catalyst after a pure methanol bath (G) without and (H) with CV scans (0–1.0 V, 20 cycles).

metal-free N–C catalyst was transferred from the methanol-containing electrolyte to a methanol-free one, the ORR polarization plots showed no recovery regardless of the methanol concentration (Fig. 1F and Fig. S5, ESI†). Therefore, pyridinic N sites suffer from a stronger methanol adsorption, which induces a much more severe activity decay when compared to FeN_4 active sites.

To fully understand the methanol-induced activity decay, we conducted a series of electrochemical tests for investigating the methanol adsorption processes. The Fe–N–C catalyst was first immersed into pure methanol for 10 and 30 min, respectively, followed by being transferred back to methanol-free 0.5 M H_2SO_4 electrolyte. The ORR polarization plots almost overlapped with the one measured from the catalyst without methanol adsorption (Fig. 1G). This is different from the KSCN poisoning studies (Fig. S6, ESI†), implying that methanol could not be adsorbed onto the catalysts through chemical adsorption. Oppositely, when potential cycles (0–1.0 V *vs.* RHE for 20 cycles) were applied in the pure methanol electrolyte, the behavior is different. Compared to the Fe–N–C catalyst in fresh 0.5 M H_2SO_4, the catalyst which was subject to potential cycling in methanol solution exhibited a significant negative shift of $E_{1/2}$ along with a limiting current decay (Fig. 1H). This phenomenon evidenced that the adsorption of methanol on FeN_4 sites is related to an electrochemical process, rather than the traditional chemical or electrostatic interactions. When the Fe–N–C catalyst was transferred back to the methanol free-electrolyte, it was hard to completely remove the adsorbed methanol through simple rinsing with a methanol-free solution (Fig. 1B and C).

However, after we tried a drying treatment at 30 °C under a vacuum to remove methanol, the ORR activity of the catalyst was nearly recovered (Fig. S7, ESI†), which was not observed by merely rinsing with a methanol-free solution. This suggests that the FeN_4 sites remain intact after completely removing methanol. The methanol tolerance of the Co–N–C and Mn–N–C catalysts[13,18] was also studied in 0.5 M H_2SO_4 electrolyte containing different methanol concentrations, as depicted in Fig. S8A and B (ESI†), respectively. The Fe–N–C catalyst exhibited better methanol tolerance than that of the Co–N–C and Mn–N–C catalysts, as they displayed 3, 15, and 12 mV negative shifts of $E_{1/2}$ in an electrolyte with 1.0 M methanol, respectively.

Density functional theory (DFT) calculations were conducted to further elucidate the methanol adsorption behavior on different active sites, including pyridinic N–C and MN_4 (M = Fe, Co, and Mn). Fig. 2A illuminates the most stable adsorption modes of methanol molecules on pyridinic N and FeN_4 sites under charge-neutral and applied constant potential conditions (U = 0 and 0.8 V *vs.* RHE), respectively. The methanol adsorption modes on the CoN_4 and MnN_4 catalysts are also displayed in Fig. S9 (ESI†). As shown in Fig. 2B, FeN_4 sites have the smallest adsorption energy among the four studied ones under both the charge-neutral conditions and at constant applied potential, implying that the FeN_4 active sites possess the highest methanol tolerance ability. This theoretical prediction agrees with the above-mentioned experimental results that the FeN_4 sites presented the highest methanol resistance ability compared to the pyridinic N, CoN_4, and MnN_4 sites.

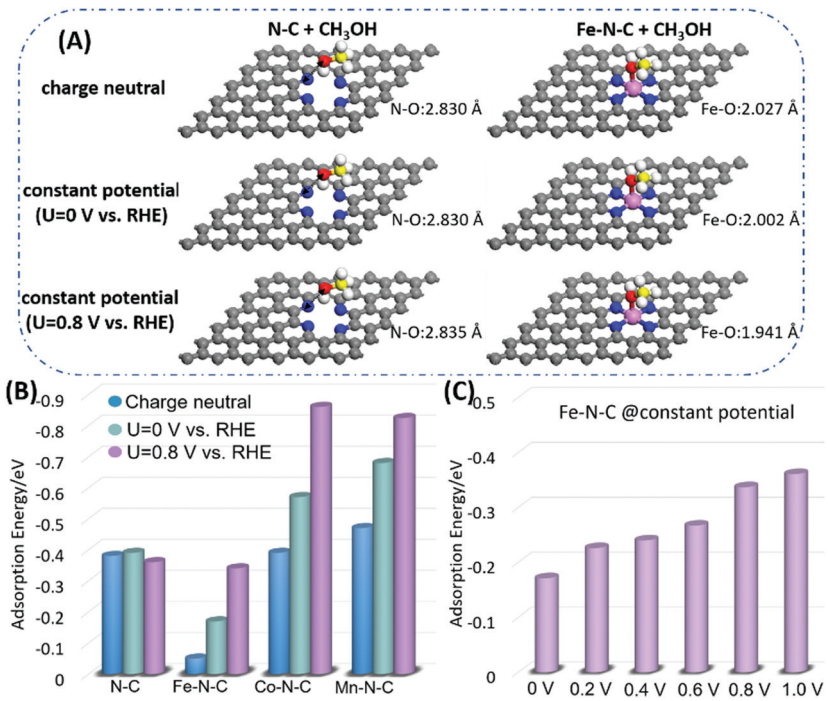

Fig. 2 (A) Adsorption mode of CH_3OH on the N–C and FeN_4 sites as obtained using DFT with the Perdew–Burke–Ernzerhof functional. (B) The adsorption energy of CH_3OH on the N–C, FeN_4, CoN_4, and MnN_4 active sites, calculated using the charge-neutral method and constant potential method at U = 0 and 0.8 V *vs.* RHE, respectively. (C) The adsorption energy of CH_3OH as a function of the applied potential for the FeN_4 sites.

As a constant potential is applied on the active sites,[43–45] the adsorption energy of the MN_4 sites increases. Oppositely, for the N–C sites, the adsorption energy remains unchanged. This indicates that the applied potential could facilitate methanol adsorption on MN_4 sites. The higher the applied potential, the stronger the methanol adsorption on the FeN_4 site (Fig. 2C), but it is still lower than the other three types of active sites. M–N–C catalysts are more sensitive to the potential than N–C catalysts, because methanol adsorption is closer to M–N–C than to N–C. As shown in Fig. 2A and Fig. S10 (ESI†), the distance from the O atom in methanol is ~2.8 Å to the nearest N atom in N–C, while ~2.0 Å to the metal atom in M–N–C. Taking the Fe–N–C catalyst as an example, Fig. S10 (ESI†) shows that, with increasing potentials, the Fermi level gradually downshifts with respect to the characteristic peaks of the Fe 3d orbital. This change in electronic state occupation alters the orbital hybridization between the metal atom and the bonded O atom in the M–N–C system, thereby changing the adsorption energy.[43–45] In contrast, for N–C, the methanol is too far away. Thus, there is no effective orbital hybridization regardless of the potential. Hence, in this case, the adsorption energy is not sensitive to the potential. These theoretical calculations are also in accordance with the experimental results that methanol adsorption on MN_4 sites is involved in the electrochemical process rather than chemical or electrostatic adsorption. Hence, the experimental and theoretical results both suggested that the Fe–N–C catalyst has enhanced methanol tolerance capability relative to N–C and other M–N–C catalysts.

Fe/Co–N–C catalyst design, synthesis, and characterization

In addition to the intrinsic activity, optimizing the porosity of M–N–C catalysts is of critical importance in boosting the mass activity through facilitating mass transfer and favoring more accessible interior active sites for the reactants.[18,33,38,46] Here, we design a binary metal site Fe/Co–N–C catalyst for modifying the porosity of the carbon support and increasing the density of FeN_4 active sites. The synthesis of Fe/Co–N–C catalysts contains a two-step chemical doping and adsorption procedure (Fig. 3A). Firstly, a Co-doped ZIF-8 crystalline precursor was prepared with a controlled Zn/Co feed ratio, followed by pyrolysis at

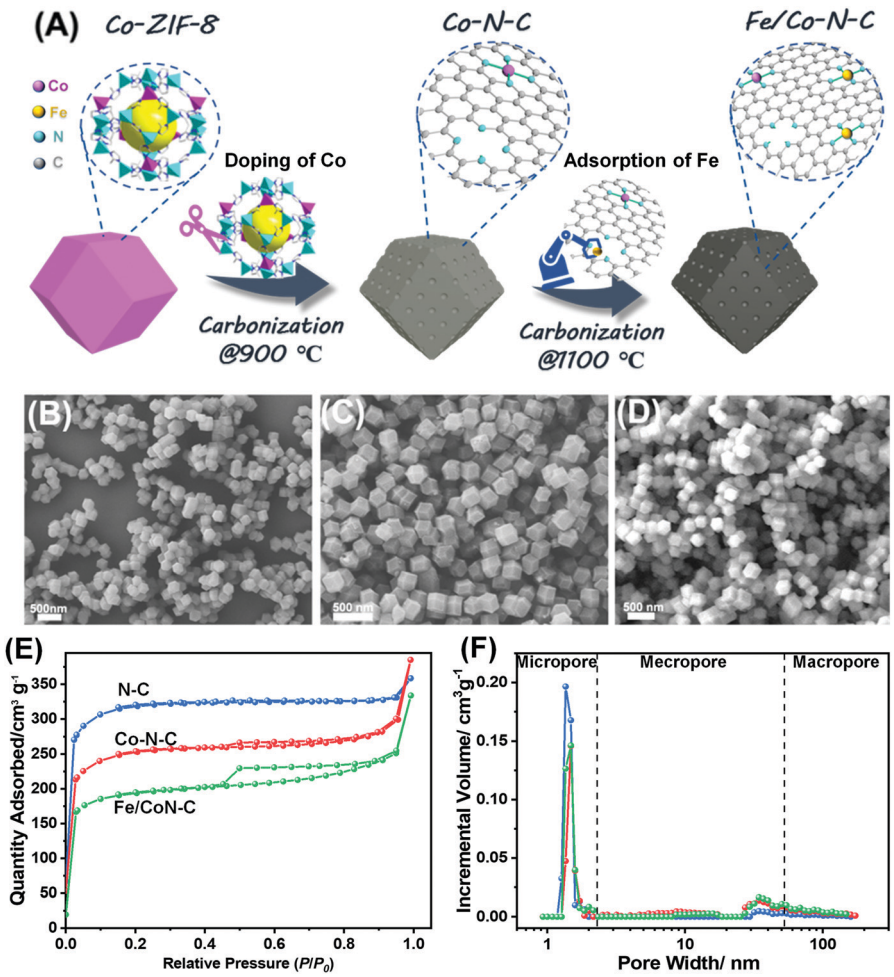

Fig. 3 (A) Schematic illustration of the Fe/Co–N–C catalyst synthesis *via* a two-step chemical doping and adsorption strategy. SEM images of (B) Co-doped ZIF-8 precursor, (C) Co-doped ZIF-8 derived Co–N–C and (D) Fe/Co–N–C catalysts. (E) Nitrogen adsorption–desorption isotherm curves and (F) pore size distribution of the N–C, Co–N–C, and Fe/Co–N–C (Zn/Co = 11/2) catalysts.

900 °C for one hour.[18] As a result, a porous and atomically dispersed Co–N–C catalyst was synthesized. Then, the Co–N–C catalyst was used as the host for subsequent Fe ion adsorption. The secondary pyrolysis at 1100 °C for one hour is to prepare an Fe/Co–N–C catalyst, dominantly containing FeN_4 active sites. Fig. 3B–D exhibit the morphologies of the Co-doped ZIF-8 nanocrystal precursor, and the Co–N–C and the Fe/Co–N–C catalyst, respectively. Their particle shapes and size were well-maintained after the two-step heat treatment, suggesting the effectiveness of achieving homogeneous catalyst morphologies by using ZIF-8 as precursors.

Due to the relatively low Co doping content, the introduction of Co does not significantly change the graphitization degree of the carbon hosts (Fig. S11, ESI†), which agrees with other similar work.[14,18] The purpose of introducing Co is not for generating a possible synergistic effect of the dual-site catalyst to improve its intrinsic activity. Instead, the doping of Co is to modify the catalyst porosity and structure. In particular, Co sites are of vital importance in acting as ''scissors'' in favoring Zn removal from the ZIF-8 precursor during the first heat treatment at 900 °C and the formation of significant mesopores. Compared to the ZIF-8-derived N–C, the Co-doped ZIF-8 derived Co–N–C is abundant in mesopores as evidenced from the nitrogen adsorption–desorption isotherm curves and pore size distribution plots in Fig. 3E and F. Importantly, the mesopore feature can be retained in the Fe/Co–N–C catalyst after the second Fe-ion adsorption and thermal activation. Meanwhile, the decreased micropore volume in the Co–N–C and Fe/Co–N–C catalysts is possibly attributed to the more efficient Zn removal facilitated by the pre-doping of Co sites. As shown in Table S1 (ESI†), the X-ray fluorescence (XRF) analysis of the Zn and Co content indicated that pre-doping of Co sites in ZIF-8 along with the second treatment can significantly reduce the residual Zn amount in the catalysts.

The Zn removal promoted by the pre-doped Co is probably attributed to the accelerated decomposition of the linkage between the metal and imidazolate.[38,47] Removing Zn atoms benefits for creating more defects for the subsequent FeN_4 site formation because increased N-coordinated sites become available for additional Fe ion adsorption in the second heating treatment. Hence, Co-doping is crucial in modifying the porosity of the catalyst for favoring mass transfer and exposing more interior active sites accessible to reactants. The porosity modification does not change the graphitization degree of the carbon support during the first heat treatment at 900 °C. Although higher temperatures, such as 1100 °C, could promote the degree of graphitization of carbon in the catalysts, they often lead to less N dopants and carbon defects (Fig. S11, ESI†).[14,18]

The Co–N–C catalyst showed a uniform size distribution of around 150–200 nm without any detectable metal clusters or nanoparticles (Fig. 4A). The optimized Zn/Co precursor feed ratio (*e.g.*, 11/2) is critical for avoiding the generation of Co aggregates. Atomically dispersed single Co sites were observed from the HAADF-STEM image in Fig. 4B. The co-existence of Co and N at the atomic level is verified by using EELS (Fig. 4C), suggesting the formation of atomically dispersed and nitrogen coordinated CoN_4 sites. The coordination number was verified by using XAS, which is discussed later. The Fe/Co–N–C catalyst inherited the morphology and size distribution of the Co–N–C catalyst after the formation of FeN_4 sites (shown in Fig. 4D and E). The surface of the Fe/Co–N–C catalysts is ''clean'' without any observable metal nanoclusters or particles, indicating well-controlled Fe adsorption content for synthesizing atomically dispersed single metal sites without generating any inactive Fe aggregates. The bright-field STEM image in Fig. 4F presents the partially graphitized carbon fringes of the Fe/Co–N–C catalyst, suggesting the formation of a stable carbon support for hosting the active sites. The HAADF-STEM images taken in different areas in Fig. 4G and H also affirmed the uniformly distributed single metal sites throughout the carbon particle. The co-existence of the Fe and N sites detected by using EELS (Fig. 4I) strongly suggested the coordination of Fe with N.

To further verify the local coordination environment of atomically dispersed Co and Fe sites in the Fe/Co–N–C catalyst,[48] X-ray absorption spectroscopy (XAS) analysis and fitting[49] were conducted (Fig. 5). The Fe K-edge X-ray absorption near edge structure (XANES) is adjacent to but on the left side of those of the FePc and Fe_2O_3 reference, suggesting that the Fe oxidization state in the catalyst is close to FePc but lower than Fe^{3+} (Fig. 5A). Similarly, the Co K-edge XANES shows that the oxidization state of Co atoms in Fe/Co–N–C is close to Co^{2+}. The Fourier transform extended X-ray absorption fine structure (EXAFS) spectra in *R*-space of Fe and Co (Fig. 5B and E) display a primary peak around 1.5 Å, which stands for Fe–N/C and Co–N/C bonds, respectively. Compared with Fe and Co metal foil, there is no apparent metal–metal scattering peak around 2.1 Å for the Fe/Co–N–C catalyst, which indicates no Fe or Co metallic cluster formation. These results are consistent with the STEM findings and confirm that both Fe and Co sites are atomically dispersed into the carbon matrix. Furthermore, the modeled EXAFS fitting (Fig. 5B, C, E and F) also confirms that Fe and Co do not have any metal–metal bonds. The EXAFS fitting results using FePc and CoPc as the standard models (Tables S3 and S4, ESI†) conclude that the average coordination numbers of Fe–N and Co–N are 3.9 ± 0.7 and 4.6 ± 1.2, respectively. Given the acceptable error bar, the XAS fitting analysis further confirms the formation of well-defined CoN_4 and FeN_4 moieties in the Fe/Co–N–C catalysts.

Rotating ring-disk electrode (RRDE) tests were firstly conducted for evaluating the ORR activity of the Fe/Co–N–C catalyst in 0.5 M H_2SO_4 electrolyte. The best-performing Fe/Co–N–C catalyst was obtained by adjusting the precursor feed ratio of Zn/Co in the first chemical Co-doping step and the content of Fe ions used for the second adsorption step. Fig. 6A indicates that the optimized Zn/Co precursor feed ratio was 11/2. Excessive Co-doping with a Zn/Co ratio up to 9/4 may result in the formation of inactive Co-based metal species, as displayed in Fig. S12 (ESI†). An atomically dispersed Fe–N–C (13 : 0) catalyst with a similar size was synthesized through identical procedures except for the pre-doping of Co-atoms at the first step for a comparison. The ORR polarization curve of the Fe–N–C catalyst almost overlapped with the optimal Fe/Co–N–C catalyst

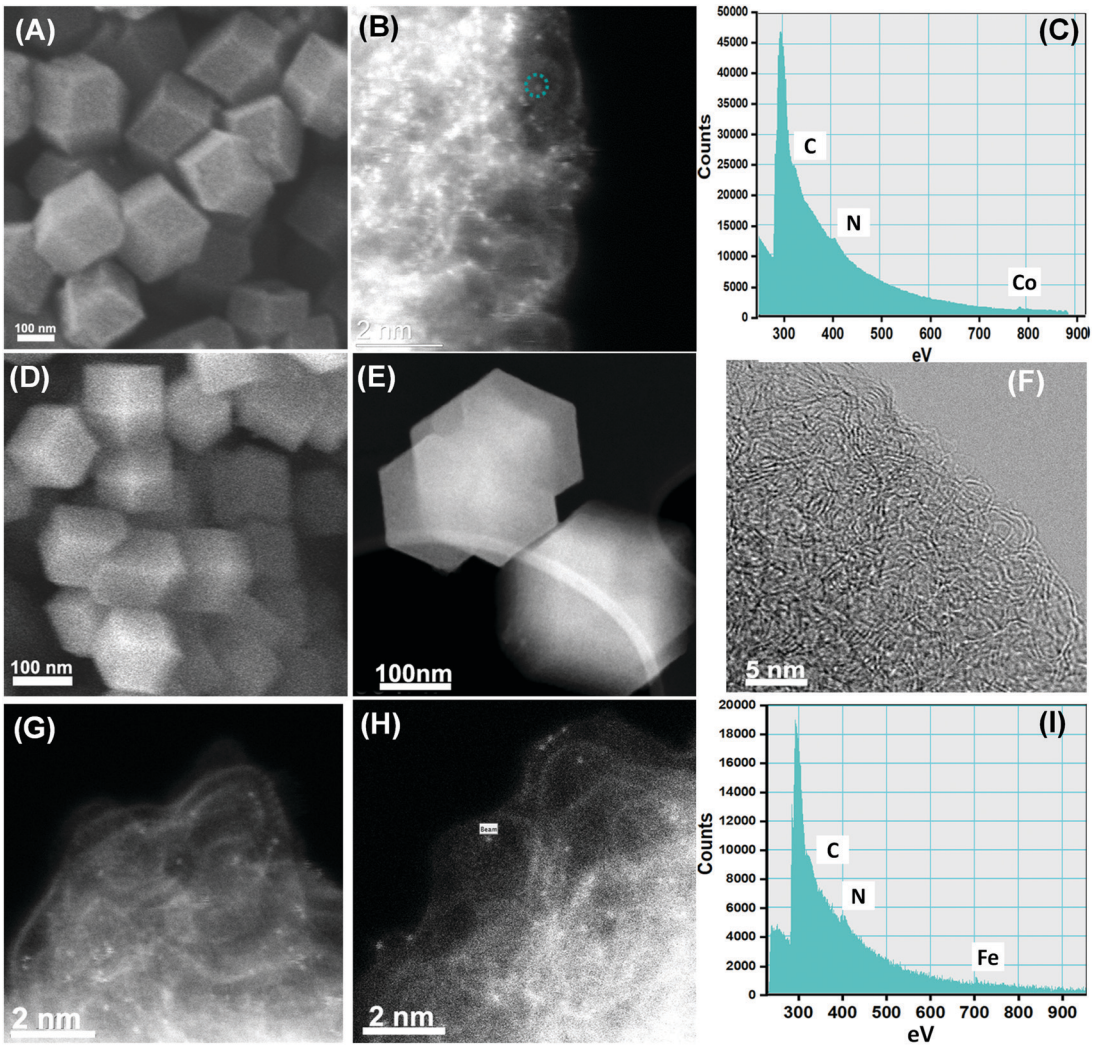

Fig. 4 (A) SEM images, (B) HAADF-STEM image, and (C) EELS analysis of the Co-doped ZIF-8-derived Co–N–C catalyst. (D) SEM, (E) STEM, (F) HRTEM, (G and H) HAADF-STEM, and (I) EELS analysis of the Fe/Co–N–C catalyst (Zn/Co = 11/2).

in the kinetically-controlled potential range (Fig. 6A), suggesting no apparent synergy between CoN_4 and FeN_4 sites. However, the larger limiting current of the Fe/Co–N–C catalyst revealed that it possesses a higher surface area and a better mass transfer than those of the Fe–N–C catalyst without Co-doping. Through adjusting the content of the Fe ion precursor (*i.e.*, 3.5 mg $FeCl_3$), the Fe/Co–N–C catalyst achieved an $E_{1/2}$ of 0.85 V *vs.* RHE at a catalyst loading of 0.6 mg cm^{-2} and a rotation speed of 900 rpm in 0.5 M H_2SO_4 electrolyte (Fig. 6B). Similarly, a low amount of Fe leads to an insufficient number of active sites. In contrast, an excessive one results in the formation of inactive Fe nanoclusters, which cause adverse ORR activity. The optimized Fe/Co–N–C catalysts outperformed the previously reported Fe/Co–N–C catalysts[38] and are comparable to most of the Fe–N–C catalysts.[14] The density of active sites can be quantified by the CO-stripping[50,51] and nitrite reduction stripping methods.[52] Here we conducted a nitrite stripping experiment for evidencing the increased number of active sites in the Fe/Co–N–C (11/2) catalyst. Based on the CV curves in Fig. S13 (ESI†), the as-calculated gravimetric site density for the Fe/Co–N–C is around 17.8 μmol g^{-1}, which is higher than that of the Fe–N–C (11.2 μmol g^{-1}). Thus, the effective removal of Zn atoms, due to the pre-doping of Co, created more N-coordinated defects for the subsequent Fe adsorption, leading to an increased density of FeN_4 active sites accessible to reactants.

Aside from the improved catalytic activity in the acidic electrolyte, the Fe/Co–N–C catalyst also demonstrated excellent stability with only a 20 mV $E_{1/2}$ loss after 10 000 cycles duirng a potential cycling test between 0.6 and 1.0 V in O_2 saturated 0.5 M H_2SO_4 electrolyte, as shown in Fig. S14A (ESI†). Besides, the Fe/Co–N–C catalyst retained up to 80% of its initial current density after a 15 hours chronoamperometry test at a challenging potential of 0.83 V in the same electrolyte (Fig. S14B, ESI†), showing improved stability relative to the Fe–N–C tested under a similar condition.[36] Although the stability tests may not be long enough, most of the activity loss of M–N–C catalysts occurs at the initial stage during the ORR. We did not identify an increased degree of graphitization of carbon in the Fe/Co–N–C

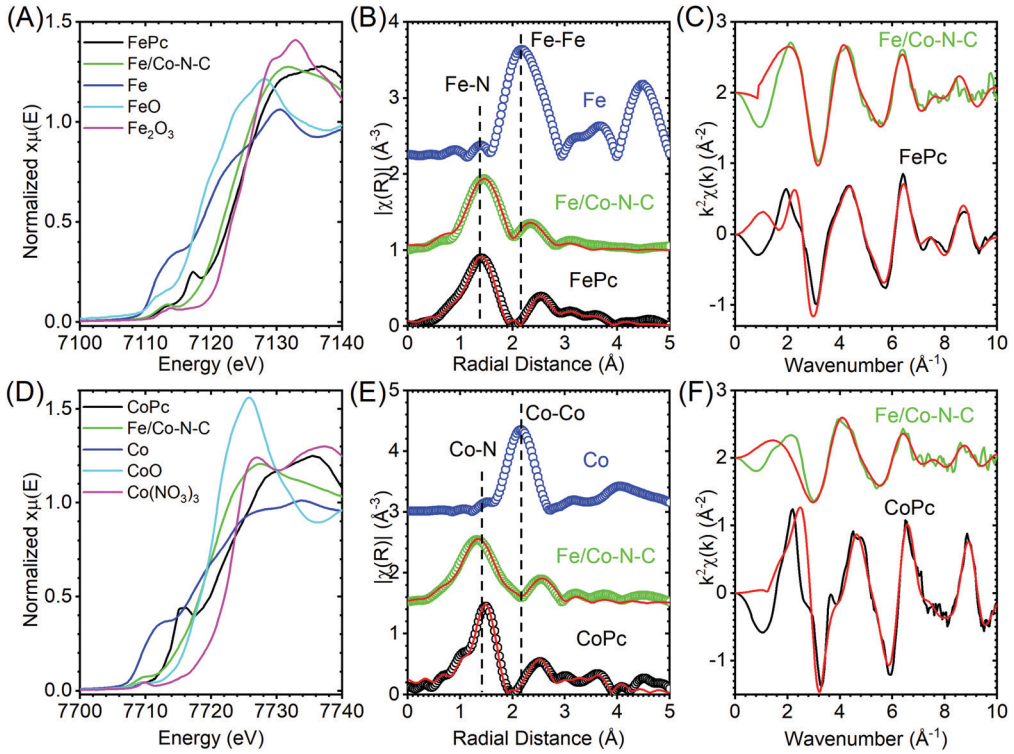

Fig. 5 (A–C) Fe K-edge XANES spectra, fit of the Fourier transform *R*-space EXAFS, and fit of the *k*-space EXAFS, and (D–F) Co K-edge XANES spectra, fit of the Fourier transform *R*-space EXAFS, and fit of the *k*-space EXAFS.

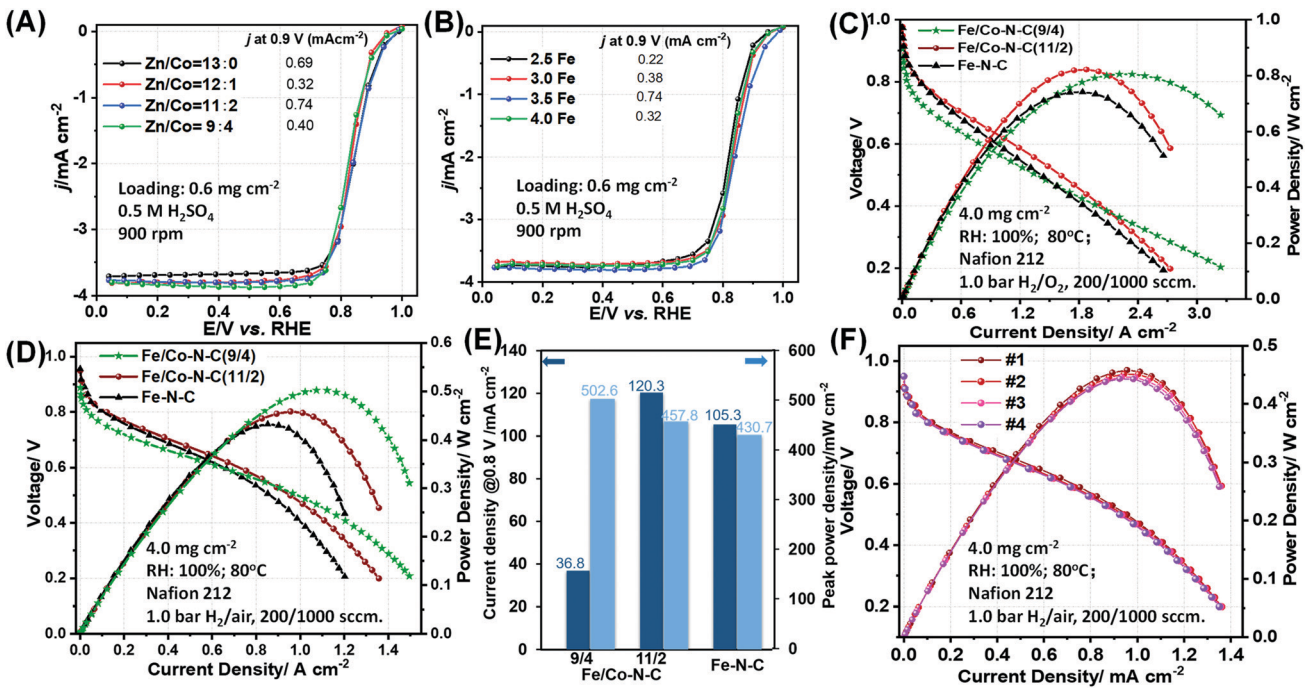

Fig. 6 ORR polarization plots of Fe/Co–N–C catalysts (A) with a constant Fe feed dose (3.5Fe) and different Co-doping ratios, and (B) with a constant Co-doping ratio (11/2) and different Fe adsorption content. Polarization plots of (C) H_2–O_2 and (D) H_2–air cells using two Fe/Co–N–C and the Fe–N–C catalysts, respectively. (E) Comparison of the current density at 0.8 V and peak power density of three studied catalysts in H_2–air fuel cells. (F) The insignificant performance degradation during four times of continuous scanning.

catalyst when compared to ZIF-8 derived N–C and Fe–N–C catalysts. Thus, it remains a puzzle to clearly explain why the Fe/Co–N–C catalyst is more stable than Fe–N–C. We always observed enhanced stability of Co–N–C relative to Fe–N–C catalysts.[11]

Hence, the enhanced stability probably benefited from the intrinsically stable CoN_4 sites and their possible interaction with adjacent FeN_4 sites.[34] To determine the importance of the sequence to introduce Co and Fe in the dual site catalyst, we designed a control experiment to synthesize a Co/Fe–N–C catalyst by pre-doping Fe first into the ZIF-8 precursor and then performing adsorption of Co ions at the second step, followed by identical heating procedures. The morphology and size are similar to Fe/Co–N–C (Fig. S15A, ESI†). However, the Co/Fe–N–C catalyst is inferior to the optimal Fe/Co–N–C catalyst (pre-doped Co and then Fe ion adsorption second) (Fig. S15B, ESI†). The comparison further highlights the significance of pre-doping Co at the first step, which is critical for enhancing the catalyst performance of the dual-site Fe/Co–N–C catalyst.

Two Fe/Co–N–C catalysts (with Zn/Co ratios of 9/4 and 11/2) were selected for further MEA studies in both H_2–oxygen/air and methanol–air fuel cells. The aim of studying the H_2–oxygen/air cells is to investigate the actual ORR activity of Fe/Co–N–C catalysts in MEAs with enhanced mass transport. Also, based on the baseline performance of MEAs under H_2–air conditions, we can determine the possible polarization loss at the anode in DMFCs due to the sluggish MOR. Fig. 6C presents the H_2–O_2 cell performance for the two Fe/Co–N–C (9/4 and 11/2) catalysts and the Fe–N–C (13/0) catalyst.

Both Fe/Co–N–C catalysts conveyed higher power densities of 800 mW cm^{-2} when compared to the Fe–N–C catalyst (740 mW cm^{-2}) under H_2–O_2 conditions. In the whole voltage range, the Fe/Co–N–C (11/2) catalyst performs better than the single site Fe–N–C catalyst although they exhibited simialr ORR activity in RDE tests, further confirming enhanced fuel cell performance by using the dual-site Co and Fe, relative to individual Fe. Then MEA performance under more practical H_2–air conditions was assessed, and the corresponding *VI* polarization plots are shown in Fig. 6D. Two performance metrics, including the current density at 0.8 V and peak power densities, are summarized in Fig. 6E for the studied three catalysts. The power density of the MEA with the Fe/Co–N–C (9/4) catalyst reached 502 mW cm^{-2}, while the value decreased to 458 mW cm^{-2} as the Co-doping content reduced to 11/2. The Fe–N–C control catalyst generated a relatively lower peak power density of 435 mW cm^{-2}. Thus, these values measured with two Fe/Co–N–C catalysts are significantly higher than most of the current M–N–C cathodes (Table S2, ESI†).[14,18,38,53–56] Although achieving a slightly lower power density relative to the Fe/Co–N–C (9/4), the Fe/Co–N–C (11/2) with optimized Co-content exhibited the highest current density of 120.3 mA cm^{-2} at 0.8 V, which is approaching the U.S. DOE target (150 mA cm^{-2}). Even though the Fe–N–C (13 : 0) catalyst possesses similar intrinsic activity to Fe/Co–N–C (11/2) in the RDE test, it conveys inferior performance in both the kinetic and mass transport region under H_2–air conditions (*e.g.*, 105 mA cm^{-2} at 0.8 V). The reason could be attributed to a higher Brunauer–Emmett–Teller (BET) surface area and a larger extent of mesopores in the Fe/Co–N–C catalyst (807.6 m^2 g^{-1}) than that in the Fe–N–C catalyst (620.7 m^2 g^{-1}), as evidenced in the nitrogen adsorption–desorption isotherm curves and pore size distribution plots displayed in Fig. S16 (ESI†). Thus, the pre-doping of Co is beneficial for creating significant mesopores and favoring O_2 diffusion to a larger number of FeN_4 sites within the thick 3D cathode. These results further highlighted the importance of the catalyst structure and porosity in optimizing the MEA performance especially under air conditions, which is more complex than the simple RDE test in aqueous electrolytes. Importantly, the Fe/Co–N–C (11/2) catalyst maintained the performance with negligible variation during four continuous tests (Fig. 6F), manifesting its considerable stability.

Inspired by the remarkably enhanced MEA performance in H_2–air cells as well as the intrinsic methanol tolerance of M–N–C catalysts, the best performing Fe/Co–N–C catalyst was studied in a methanol–air cell with a series of methanol feed concentrations. Fig. 7A and B present the polarization plots of DMFCs using both the Fe/Co–N–C (11/2) and a commercial Pt/C cathode. Polarization plots at the same methanol concentration were continuously recorded twice (Fig. S17, ESI†). This is to verify that the performance difference is caused by the methanol feed concentrations rather than catalyst activity decay. Their open-circuit voltages (OCV) under different methanol concentrations are compared in Fig. 7C. The MEA using the Fe/Co–N–C catalyst achieved an OCV of 0.87 V at 1.0 M methanol at the anode. When the methanol concentration is increased from 0.5 to 2.0 M, the corresponding OCVs and performance of the MEAs remained nearly unchanged. A higher concentration of methanol beyond 3.0 M results in a slight performance decrease, especially in the mass transport region (Fig. 7D). In contrast, the OCV of the MEA using the Pt/C cathode only reached 0.7 V, implying a significant voltage loss due to the mixed potential from the ORR and the MOR at the cathode (Fig. 7B). Also, with an increase of the methanol concentration, OCVs and MEA performance of the Pt/C cathode suffer from a continuous and rapid drop (Fig. 7B and E). The measured power densities of these two MEAs using the Fe/Co–N–C and Pt/C cathodes are compared in Fig. 7F. A maximum peak power density of 135 mW cm^{-2} was achieved at 1.0 M for the Fe/Co–N–C (11/2) cathode, but it slightly decreases at higher concentration (*e.g.*, 106 mW cm^{-2} at 4.0 M). In contrast, the peak power density of the Pt/C cathode experienced severe degradation as the methanol concentration increased from 0.5 M (80 mW cm^{-2}) to 4.0 M (31 mW cm^{-2}). The comparison validates the good methanol tolerance of the Fe/Co–N–C catalyst in DMFCs. However, it should be noted that there is still noticeable performance degradation in the mass transfer region for the Fe/Co–N–C cathode. As we fundamentally elucidated by using RDE tests, both FeN_4 and CoN_4 sites are not completely methanol tolerant. They still suffer from ORR activity loss in aqueous electrolytes due to methanol adsorption, especially during the high potentials for the ORR. Also, the effects of methanol on the proton conductivity and O_2 diffusion rates within ionomers may cause performance degradation of MEAs.[39,40,57] Besides, excessive methanol may generate water flooding issues.[57,58] However, compared to traditional Pt/C cathodes, the degradation in the mass transfer region is significantly alleviated by using the Fe/Co–N–C cathode. The performance of the Fe–N–C catalyst was also studied in a methanol–air cell. The Fe–N–C catalyst delivered a lower peak

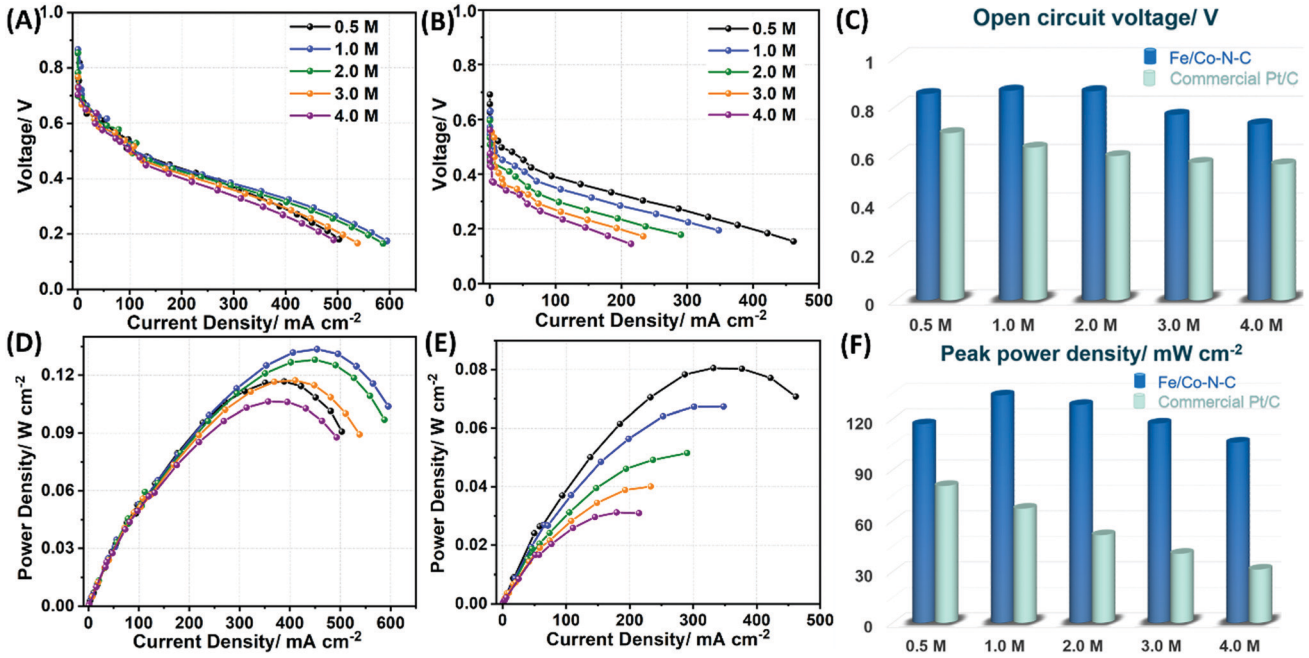

Fig. 7 Polarization plots of the (A and B) cell voltage and (D and E) power density *versus* current density of the methanol–air cell using Fe/Co–N–C (11/2) (A and D) and commercial Pt/C (B and E) as cathode catalysts as a function of methanol concentration. (C) OCV and (F) peak power density of the Fe/Co–N–C (11/2) and commercial Pt/C catalysts used as cathode catalysts in the methanol–air cell. Anode: 4.0 mg cm^{-2} PtRu/C; cathode: 5.0 mg cm^{-2} Fe/Co–N–C (11/2) or 0.9 mg cm^{-2} Pt/C; 0.5 mL min^{-1} methanol flow rate; 1.0 atm air 1000 mL min^{-1} flow rate; membrane: Nafion 212; cell: 80 °C.

power density of 124 mW cm^{-2} (Fig. S18, ESI†) than the optimal Fe/Co–N–C (135 mW cm^{-2}). This further confirms that the optimal Fe/Co–N–C catalyst, which has favorable porosity and morphology for improved mass transport, is superior to single-site Fe–N–C catalysts in DMFCs.

When compared to all reported DMFC performances, the achieved peak power density in this work is the highest using a PGM-free cathode (Fig. S19, ESI†).[6,9,59–62] The encouraging performance may be due to multiple factors, including the enhanced intrinsic ORR activity of the atomically dispersed FeN_4 and CoN_4 sites, outstanding methanol tolerance of PGM-free MN_4 sites, and the improved mass transport from favorable mesopores in the catalysts. Therefore, the atomically dispersed metal site catalyst would hold great promise for viable applications in DMFCs and other direct fuel cells (*e.g.*, ethanol and NH_3) with enhanced performance and durability.

Conclusions

In summary, atomically dispersed single metal site M–N–C catalysts demonstrated great promise to be high-performance PGM-free cathodes for DMFCs. At first, using a model Fe–N–C catalyst containing exclusive FeN_4 active sites, we experimentally studied its ORR behavior as a function of methanol concentrations. When the methanol concentration is lower than 2.0 M, the effect of methanol on the ORR is negligible. Higher methanol concentrations over 4.0 M cause a noticeable irreversible decay in ORR activity due to the strong adsorption of methanol, especially in an electrochemical environment. Combined with DFT calculations, we further elucidated that FeN_4 sites have relatively weaker methanol adsorption when compared to pyridinic N, CoN_4, and MnN_4 active sites. Adsorption of methanol on pyridinic N is independent of the applied potential. In contrast, the adsorption on MN_4 sites is dependent mainly on the applied electrode potentials and becomes stronger at higher potentials. However, the methanol adsorption does not affect the $4e^-$ ORR pathway and destroy the structure of the FeN_4 site.

Due to the exceptional methanol tolerance of Fe–N–C catalysts, we rationally designed an atomically dispersed dual-site Fe/Co–N–C catalyst *via* a two-step synthesis approach combining chemical Co-doping into ZIF-8 and subsequent Fe ion adsorption, along with a separate heat treatment after each step. Instead of the possible synergy between Fe and Co, we discovered that the pre-doping of Co at the first step is crucial for adjusting the porosity of the carbon host and enhancing the catalyst stability. The Fe/Co–N–C catalyst with optimal metal precursor content exclusively contains atomically dispersed FeN_4 and CoN_4 sites. As a result, the Fe/Co–N–C catalyst exhibited outstanding ORR activity and stability in acidic electrolyte with an $E_{1/2}$ of 0.85 V. Furthermore, the MEA using the Fe/Co–N–C cathode delivered a remarkable power density up to 502 and 135 mW cm^{-2} using 1.0 bar H_2/air and 1.0 M methanol, respectively. Unlike the significant performance loss of the traditional Pt/C cathode, the Fe/Co–N–C cathode has significantly enhanced methanol tolerance in DMFCs at the studied methanol concentrations up to 4.0 M. MEA studies further verified that the pre-chemical doping of Co atoms is the key for the formation of mesopores, which is pivotal in promoting mass transfer and maximizing

the accessibility of FeN_4 active sites in the cathode. The finely devised Fe/Co–N–C catalysts afforded a promising approach to engineering M–N–C catalysts with exceptional methanol tolerance ability and enhanced power output.

Currently, the performance gap between H_2–air and methanol–air cells is still significant for M–N–C cathode catalysts. It is due to various factors, including the insufficient anode catalytic activity, methanol poisoning on MN_4 active sites, and additional mass/charge transport resistance resulting from methanol within the cathode. Therefore, further efforts are needed to boost the M–N–C cathode performance in DMFCs through increasing the density of active sites, engineering porosity with uniform ionomer dispersion, and optimizing carbon structures for improved mass transport.

Conflicts of interest

There are no conflicts to declare.

Acknowledgements

The authors acknowledge the financial support from the U.S. Department of Energy, Office of Energy Efficiency and Renewable Energy (EERE), Fuel Cell Technology Office (DE-EE0008075, DE-EE0008076, and DE-EE0008417) and the National Science Foundation (CBET-1604392, 1804326). This research used resources of the beamline 12-BM of the Advanced Photon Source (APS), a U.S. Department of Energy (DOE) Office of Science User Facility operated for the DOE Office of Science by Argonne National Laboratory under Contract DE-AC02-06CH11357. The DFT calculations are supported by the National Science Foundation (1900039) and the Welch Foundation (F-1959-20180324). This work used computational resources at National Renewable Energy Lab, XSEDE (TG-CHE190065), Argonne National Lab, and Oak Ridge National Lab.

Notes and references

1 Z. Qiao, S. Hwang, X. Li, C. Wang, W. Samarakoon, S. Karakalos, D. Li, M. Chen, Y. He, M. Wang, Z. Liu, G. Wang, H. Zhou, Z. Feng, D. Su, J. S. Spendelow and G. Wu, *Energy Environ. Sci.*, 2019, **12**, 2830–2841.
2 S. Zhu, J. Ge, C. Liu and W. Xing, *EnergyChem*, 2019, **1**, 100018.
3 Y. Li, H. Wang, C. Priest, S. Li, P. Xu and G. Wu, *Adv. Mater.*, 2020, 2000381, DOI: 10.1002/adma.202000381.
4 X. X. Wang, M. T. Swihart and G. Wu, *Nat. Catal.*, 2019, **2**, 578–589.
5 X. Zhao, M. Yin, L. Ma, L. Liang, C. P. Liu, J. H. Liao, T. H. Lu and W. Xing, *Energy Environ. Sci.*, 2011, **4**, 2736–2753.
6 Q. Li, T. Y. Wang, D. Havas, H. G. Zhang, P. Xu, J. T. Han, J. Cho and G. Wu, *Adv. Sci.*, 2016, **3**, 1600140.
7 D. Sebastian, A. Serov, I. Matanovic, K. Artyushkova, P. Atanassov, A. S. Arico and V. Baglio, *Nano Energy*, 2017, **34**, 195–204.
8 X. Xu, Z. Xia, X. Zhang, H. Li, S. Wang and G. Sun, *Nanoscale*, 2020, **12**, 3418–3423.
9 Z. Xia, X. Xu, X. Zhang, H. Li, S. Wang and G. Sun, *J. Mater. Chem. A*, 2020, **8**, 1113–1119.
10 J. Hou, M. Yang, C. Ke, G. Wei, C. Priest, Z. Qiao, G. Wu and J. Zhang, *EnergyChem*, 2020, **2**, 100023.
11 X. X. Wang, V. Prabhakaran, Y. He, Y. Shao and G. Wu, *Adv. Mater.*, 2019, **31**, 1805126.
12 Q. Shi, S. Hwang, H. Yang, F. Ismail, D. Su, D. Higgins and G. Wu, *Mater. Today*, 2020, **37**, 93–111.
13 J. Li, M. Chen, D. A. Cullen, S. Hwang, M. Wang, B. Li, K. Liu, S. Karakalos, M. Lucero, H. Zhang, C. Lei, H. Xu, G. E. Sterbinsky, Z. Feng, D. Su, K. L. More, G. Wang, Z. Wang and G. Wu, *Nat. Catal.*, 2018, **1**, 935–945.
14 J. Li, H. Zhang, W. Samarakoon, W. Shan, D. A. Cullen, S. Karakalos, M. Chen, D. Gu, K. L. More, G. Wang, Z. Feng, Z. Wang and G. Wu, *Angew. Chem., Int. Ed.*, 2019, **58**, 18971–18980.
15 H. G. Zhang, S. Hwang, M. Y. Wang, Z. X. Feng, S. Karakalos, L. L. Luo, Z. Qiao, X. H. Xie, C. M. Wang, D. Su, Y. Y. Shao and G. Wu, *J. Am. Chem. Soc.*, 2017, **139**, 14143–14149.
16 Y. He, S. Hwang, D. A. Cullen, M. A. Uddin, L. Langhorst, B. Li, S. Karakalos, A. J. Kropf, E. C. Wegener, J. Sokolowski, M. Chen, D. Myers, D. Su, K. L. More, G. Wang, S. Litster and G. Wu, *Energy Environ. Sci.*, 2019, **12**, 250–260.
17 G. Zhang, X. Yang, M. Dubois, M. Herraiz, R. Chenitz, M. Lefèvre, M. Cherif, F. Vidal, V. P. Glibin, S. Sun and J.-P. Dodelet, *Energy Environ. Sci.*, 2019, **12**, 3015–3037.
18 Q. Shi, C. Zhu, D. Du and Y. Lin, *Chem. Soc. Rev.*, 2019, **48**, 3181–3192.
19 G. Wu, K. L. More, C. M. Johnston and P. Zelenay, *Science*, 2011, **332**, 443–447.
20 M. Xiao, H. Zhang, Y. Chen, J. Zhu, L. Gao, Z. Jin, J. Ge, Z. Jiang, S. Chen, C. Liu and W. Xing, *Nano Energy*, 2018, **46**, 396–403.
21 M. Chen, Y. He, J. S. Spendelow and G. Wu, *ACS Energy Lett.*, 2019, **4**, 1619–1633.
22 D. Sebastián, V. Baglio, A. S. Aricò, A. Serov and P. Atanassov, *Appl. Catal., B*, 2016, **182**, 297–305.
23 L. Yang, D. Cheng, H. Xu, X. Zeng, X. Wan, J. Shui, Z. Xiang and D. Cao, *Proc. Natl. Acad. Sci. U. S. A.*, 2018, **115**, 6626–6631.
24 B. You, N. Jiang, M. Sheng, W. S. Drisdell, J. Yano and Y. Sun, *ACS Catal.*, 2015, **5**, 7068–7076.
25 Y. Ma, S. Luo, M. Tian, J. E. Lu, Y. Peng, C. Desmond, Q. Liu, Q. Li, Y. Min and Q. Xu, *J. Power Sources*, 2020, **450**, 227659.
26 S. Mukherjee, X. Yang, W. Shan, W. Samarakoon, S. Karakalos, D. A. Cullen, K. More, M. Wang, Z. Feng, G. Wang and G. Wu, *Small Methods*, 2020, **4**, 1900821.
27 C. Zhu, S. Fu, Q. Shi, D. Du and Y. Lin, *Angew. Chem., Int. Ed.*, 2017, **56**, 13944–13960.
28 A. Zitolo, V. Goellner, V. Armel, M.-T. Sougrati, T. Mineva, L. Stievano, E. Fonda and F. Jaouen, *Nat. Mater.*, 2015, **14**, 937–942.
29 T. Asset and P. Atanassov, *Joule*, 2020, **4**, 33–44.
30 J.-C. Li, S. Maurya, Y. S. Kim, T. Li, L. Wang, Q. Shi, D. Liu, S. Feng, Y. Lin and M. Shao, *ACS Catal.*, 2020, **10**, 2452–2458.

31 J.-C. Li, F. Xiao, H. Zhong, T. Li, M. Xu, L. Ma, M. Cheng, D. Liu, S. Feng, Q. Shi, H.-M. Cheng, C. Liu, D. Du, S. P. Beckman, X. Pan, Y. Lin and M. Shao, *ACS Catal.*, 2019, **9**, 5929–5934.
32 Y. Mun, S. Lee, K. Kim, S. Kim, S. Lee, J. W. Han and J. Lee, *J. Am. Chem. Soc.*, 2019, **141**, 6254–6262.
33 R. Jiang, L. Li, T. Sheng, G. Hu, Y. Chen and L. Wang, *J. Am. Chem. Soc.*, 2018, **140**, 11594–11598.
34 Y. Shao, J. P. Dodelet, G. Wu and P. Zelenay, *Adv. Mater.*, 2019, **31**, 1807615.
35 Y. He, S. Liu, C. Priest, Q. Shi and G. Wu, *Chem. Soc. Rev.*, 2020, **49**, 3484–3524.
36 H. Zhang, H. T. Chung, D. A. Cullen, S. Wagner, U. I. Kramm, K. L. More, P. Zelenay and G. Wu, *Energy Environ. Sci.*, 2019, **12**, 2548–2558.
37 Y. Zhu, J. Sokolowski, X. Song, Y. He, Y. Mei and G. Wu, *Adv. Energy Mater.*, 2020, **10**, 1902844.
38 J. Wang, Z. Huang, W. Liu, C. Chang, H. Tang, Z. Li, W. Chen, C. Jia, T. Yao and S. Wei, *J. Am. Chem. Soc.*, 2017, **139**, 17281–17284.
39 A. L. Ocampo, R. H. Castellanos and P. J. Sebastian, *J. New Mater. Electrochem. Syst.*, 2002, **5**, 163–168.
40 R. N. Itoe, G. D. Wesson and E. E. Kalu, *J. Electrochem. Soc.*, 2000, **147**, 2445–2450.
41 I. Martinaiou, A. H. M. Videla, N. Weidler, M. Kübler, W. D. Z. Wallace, S. Paul, S. Wagner, A. Shahraei, R. W. Stark and S. Specchia, *Appl. Catal., B*, 2020, **262**, 118217.
42 C. Zhu, Q. Shi, B. Z. Xu, S. Fu, G. Wan, C. Yang, S. Yao, J. Song, H. Zhou and D. Du, *Adv. Energy Mater.*, 2018, **8**, 1801956.
43 D. Kim, J. Shi and Y. Liu, *J. Am. Chem. Soc.*, 2018, **140**, 9127–9131.
44 X. Zhao and Y. Liu, *J. Am. Chem. Soc.*, 2020, **142**, 5773–5777.
45 X. Zhao, J. Shi, Y. Ji and Y. Liu, *Wiley Interdiscip. Rev.: Comput. Mol. Sci.*, 2019, **9**, e1418.
46 A. Uddin, L. Dunsmore, H. Zhang, L. Hu, G. Wu and S. Litster, *ACS Appl. Mater. Interfaces*, 2020, **12**, 2216–2224.
47 M. Knez, R. Scholz, K. Nielsch, E. Pippel, D. Hesse, M. Zacharias and U. Gösele, *Nat. Mater.*, 2006, **5**, 627–631.
48 M. Wang, L. Árnadóttir, Z. J. Xu and Z. Feng, *Nano-Micro Lett.*, 2019, **11**, 47.
49 Z. Feng, Q. Ma, J. Lu, H. Feng, J. Elam, P. C. Stair and M. J. Bedzyk, *RSC Adv.*, 2015, **5**, 103834–103840.
50 F. Luo, A. Roy, L. Silvioli, D. A. Cullen, A. Zitolo, M. T. Sougrati, I. C. Oguz, T. Mineva, D. Teschner, S. Wagner, J. Wen, F. Dionigi, U. I. Kramm, J. Rossmeisl, F. Jaouen and P. Strasser, *Nat. Mater.*, 2020, 1–9.
51 N. R. Sahraie, U. I. Kramm, J. Steinberg, Y. Zhang, A. Thomas, T. Reier, J.-P. Paraknowitsch and P. Strasser, *Nat. Commun.*, 2015, **6**, 1–9.
52 M. Primbs, Y. Sun, A. Roy, D. Malko, A. Mehmood, M.-T. Sougrati, P.-Y. Blanchard, G. Granozzi, T. Kosmala and G. Daniel, *Energy Environ. Sci.*, 2020, **13**, 2480–2500.
53 X. X. Wang, D. A. Cullen, Y. T. Pan, S. Hwang, M. Wang, Z. Feng, J. Wang, M. H. Engelhard, H. Zhang, Y. He, Y. Shao, D. Su, K. L. More, J. S. Spendelow and G. Wu, *Adv. Mater.*, 2018, **30**, 1706758.
54 X. Fu, P. Zamani, J. Y. Choi, F. M. Hassan, G. Jiang, D. C. Higgins, Y. Zhang, M. A. Hoque and Z. Chen, *Adv. Mater.*, 2017, **29**, 1604456.
55 H. T. Chung, D. A. Cullen, D. Higgins, B. T. Sneed, E. F. Holby, K. L. More and P. Zelenay, *Science*, 2017, **357**, 479–484.
56 X. Fu, F. M. Hassan, P. Zamani, G. Jiang, D. C. Higgins, J.-Y. Choi, X. Wang, P. Xu, Y. Liu and Z. Chen, *Nano Energy*, 2017, **42**, 249–256.
57 D. Sebastián, A. Serov, K. Artyushkova, J. Gordon, P. Atanassov, A. S. Aricò and V. Baglio, *ChemSusChem*, 2016, **9**, 1986–1995.
58 A. H. M. Videla, D. Sebastián, N. S. Vasile, L. Osmieri, A. S. Aricò, V. Baglio and S. Specchia, *Int. J. Hydrogen Energy*, 2016, **41**, 22605–22618.
59 A. L. M. Reddy, N. Rajalakshmi and S. Ramaprabhu, *Carbon*, 2008, **46**, 2–11.
60 X. Xu, Z. Xia, X. Zhang, R. Sun, X. Sun, H. Li, C. Wu, J. Wang, S. Wang and G. Sun, *Appl. Catal., B*, 2019, **259**, 118042.
61 Y.-C. Wang, L. Huang, P. Zhang, Y.-T. Qiu, T. Sheng, Z.-Y. Zhou, G. Wang, J.-G. Liu, M. Rauf and Z.-Q. Gu, *ACS Energy Lett.*, 2017, **2**, 645–650.
62 Y. He, Q. Tan, L. Lu, J. Sokolowski and G. Wu, *Electrochem. Energy Rev.*, 2019, **2**, 231–251.

